

A Large-Scale Semi-Chronic Microdrive Recording System for Non-Human Primates

Highlights

- Large-scale recording system with up to 256 microelectrodes
- Independently moveable microelectrodes with up to 41 mm of travel
- Recording system was stable over many months
- Enables the study of large-scale networks underlying cognition

Authors

Nicholas M. Dotson,
Steven J. Hoffman, Baldwin Goodell,
Charles M. Gray

Correspondence

cmgray.montana@gmail.com

In Brief

Dotson et al. developed and implemented a large-scale, semi-chronic microdrive recording system for non-human primates. Devices remained on the monkeys for up to 9 months, and they were able to make simultaneous recordings from up to 37 cortical and subcortical areas.



A Large-Scale Semi-Chronic Microdrive Recording System for Non-Human Primates

Nicholas M. Dotson,^{1,2} Steven J. Hoffman,^{1,2} Baldwin Goodell,¹ and Charles M. Gray^{1,3,*}

¹Department of Cell Biology and Neuroscience, Montana State University, Bozeman, MT 59717, USA

²These authors contributed equally

³Lead Contact

*Correspondence: cmgray.montana@gmail.com

<https://doi.org/10.1016/j.neuron.2017.09.050>

SUMMARY

Multi-electrode recordings in the non-human primate provide a critical method for measuring the widely distributed activity patterns that underlie brain function. However, common techniques rely on small, often immovable arrays, or microdrives, that are only capable of manipulating a small number of closely spaced probes. These techniques restrict the number of cortical areas that can be simultaneously sampled and are typically not capable of reaching subcortical targets. To overcome these limitations, we developed a large-scale, semi-chronic microdrive recording system with up to 256 independently movable microelectrodes spanning an entire cerebral hemisphere. The microdrive system is hermetically sealed, free of internal connecting wires, and has been used to simultaneously record from up to 37 cortical and subcortical areas in awake behaving monkeys for up to 9 months. As a proof of principle, we demonstrate the capability of this technique to address network-level questions using a graph theoretic analysis of functional connectivity data.

INTRODUCTION

Understanding how the concerted actions of large-scale neural circuits mediate cognitive functions is one of the major challenges in neuroscience. Conventional methods for monitoring neuronal activity in non-human primates usually involve acute recordings from one to several 10s of electrodes that are advanced into and then removed from the brain each day. The electrodes are typically advanced through the dural membrane or within guide tubes that are inserted at the same time (Mountcastle et al., 1991; Prut et al., 1998; Asaad et al., 2000; Purushothaman et al., 2006; Gray et al., 2007; Buschman and Miller, 2007; Miller and Wilson, 2008; Hernández et al., 2008). While this technique has been very effective, it requires bulky, often expensive, micromanipulators that involve long setup times

and can increase the vulnerability of the animals to infection. Moreover, this approach precludes the possibility of recording from the same units over longer periods of time.

These constraints have led to the development of chronically implanted arrays of microelectrodes. In these methods, groups of individual micro-wires (Fries et al., 1997; Roelfsema et al., 1997; Donoghue et al., 1998), arrays of rigidly linked micro-wires (Nicolleis et al., 1997, 2003; Musallam et al., 2007), or fabricated silicon electrode arrays (Nordhausen et al., 1996; Rousche et al., 2001; Maynard et al., 1999; Kipke et al., 2003; Vetter et al., 2004; Kim et al., 2006; Dickey et al., 2009) are chronically implanted. The implants are designed to either float with the pulsations of the brain or be rigidly mounted to the skull. While useful for making long-term recordings, these methods also suffer from several limitations. Once the electrodes are in place, they can no longer be repositioned to isolate new activity. Thus, the experimenter is confined to studying only one set of neurons, and if neuronal activity on a particular electrode is not well isolated, or the signal is lost, that electrode can no longer yield useful data. It is also very difficult to access deep structures within the brain if large numbers of rigidly linked electrodes are being implanted.

A second approach has utilized miniature microdrives that allow the implantation and positional control of large numbers of microelectrodes. These methods improve upon the static, irreversible implants by retaining varying degrees of control over the positioning of the probes. Some methods enable position control for each individual probe (Wilson and McNaughton, 1993; deCharms et al., 1999; Venkatachalam et al., 1999; Erickson and Desimone, 1999; Vos et al., 1999; Fee and Leonardo, 2001; Szabó et al., 2001; Swadlow et al., 2005; Tolia et al., 2007; Eliades and Wang, 2008; Battaglia et al., 2009; Kloosterman et al., 2009; Nguyen et al., 2009), while others employ single or multiple devices to position arrays of electrodes together (Csicsvari et al., 2003; Krupa et al., 2004; Schwarz et al., 2014; Mendoza et al., 2016). Both approaches have been effective, but in general, most of the microdrives have been designed to manipulate a relatively small number of closely spaced probes. This limits the number of neurons and brain regions that can be simultaneously recorded (see Hoffman and McNaughton, 2002, Feingold et al., 2012, and Schwarz et al., 2014 for notable exceptions).

There are several obstacles to overcome in developing microdrive systems that can routinely record from large numbers of

sites spanning widely distributed cortical and subcortical circuits. First, it becomes increasingly difficult to make large numbers of reliable electrical connections. In small systems, electrical connections are established by bonding or soldering flexible wires to each probe (e.g., [Nguyen et al., 2009](#)). The wires must have sufficient length to provide slack as the probe is moved. Increasing the number of probes leads to problems with packaging the many wires and the need for connectors of increasing size. Second, increasing the number of probes requires further miniaturization of the actuators. Without such improvements, the microdrives become impractically large. A third obstacle is that there is no generally accepted method for introducing large numbers of independently moveable microelectrodes over widespread regions of the primate brain. The hardware employed for rodents can be bulky and easily damaged (but see [Tolias et al., 2007](#)), and surgical placement, as well as care and maintenance, of the implant becomes difficult ([Hoffman and McNaughton, 2002](#); [Feingold et al., 2012](#)).

To overcome these obstacles, we developed a large-scale, semi-chronic microdrive recording system with miniature actuators and no internal connecting wires that spans an entire cerebral hemisphere (C.M. Gray and A.B. Goodell, 2007, Soc. Neurosci., abstract; A.B. Goodell and C.M. Gray, 2008, Soc. Neurosci., abstract; [Dotson et al., 2015](#)). This system dramatically expands the number of cortical and subcortical areas that can be recorded simultaneously. We developed and tested two different versions of the system in two non-human primates trained to perform an object-based, delayed match-to-sample task (dMTS). The first animal was implanted with a 256-channel system with 20 mm of travel for each electrode. Several revisions were made to the design of the recording system, and the second animal was implanted with a 252-channel system with actuators that permit 33 mm or 41 mm of electrode travel.

RESULTS

Large-Scale Semi-chronic Microdrive System

Developing and implementing the large-scale recording system posed several significant challenges. A microdrive system was needed to house the requisite number of actuators, each capable of independent control of an electrode at high resolution, while keeping the overall size to a minimum. A compact and reliable method was needed for connecting to the electrodes while avoiding the use of loose wires. It was necessary to hermetically seal the microdrive to eliminate leakage of fluid into the device. An enclosure was required that could be firmly anchored to the animal's skull while providing robust protection against impacts and minimizing the risk of infection. And a method was needed to gain access to the brain over an area spanning a cerebral hemisphere.

To meet these requirements, we designed two versions of a form-fitting chamber and microdrive system that was customized to each animal and that could be implanted and evaluated in stages ([Figure 1](#); [Figure S2](#)). We first constructed an MRI-based 3D model of each monkey's skull ([Figure 1A](#); [Figure S1](#)). We used the resulting model, along with the coronal sections of the brain, to determine the boundaries of the chamber wall

that would provide the greatest possible access to the left cerebral hemisphere while keeping the overall footprint to a minimum. The bottom contour of the chamber wall was matched to the cranial surface along these boundaries. This design facilitated surgical placement of the chamber and the sealing of the chamber-cranial interface with bone cement.

The microdrive system was based on an earlier design (C.M. Gray and A.B. Goodell, 2007, Soc. Neurosci., abstract; A.B. Goodell and C.M. Gray, 2008, Soc. Neurosci., abstract; [Gray and Goodell, 2011](#); [Markowitz et al., 2011](#); [Salazar et al., 2012](#); [Dotson et al., 2014, 2015](#)) scaled up to match the dimensions of the chamber ([Figures 1B and 1C](#); [Figure S2](#)). It consists of a guide array, an actuator block (top and bottom components), a printed circuit board (PCB), and a screw guide. The actuator block houses a set of linear actuators (256 in design 1, 252 in design 2), each consisting of a miniature stainless steel lead-screw, a threaded brass shuttle, and a compression spring ([Figures 1B and 1C](#); [Figure S3](#)). In the first design (used for monkey 1), each actuator provided 20 mm of electrode travel at a resolution of 8 turns/mm. The second design (used for monkey 2) incorporated actuators with 33 mm or 41 mm of electrode travel at a resolution of 5 turns/mm. In both design, the actuators were spaced at 2.34 mm intervals.

The microdrives were assembled and loaded in multiple steps using sterile procedures ([Figure 2](#)). First, each microelectrode (glass-insulated tungsten; 250 μm outer diameter; ~ 1 M Ω impedance; Alpha Omega, Inc.) was cut to a specified length and bonded to a shuttle using a heat-cured conductive epoxy (Loctite 3880) ([Figure S3C](#)). The microdrive components were assembled using machine screws after each opposing component surface was coated with a thin layer of sterile silicone grease. For design 1, the guide tubes were press fit into a counter-bored hole on the bottom of the actuator block ([Figure 1B](#), inset). Then, for both designs, each electrode/shuttle assembly was front-loaded into the actuator block using polyimide tubing to guide the electrodes into place without damaging the tips ([Figure 2A](#)). Once all electrodes were loaded, the polyimide guide tubing was removed and the PCB was fixed to the top of the actuator block. A leadscrew was passed through each hole in the PCB, rotated to capture the threads of the shuttle, and adjusted until the end of the leadscrew passed through the shuttle and became seated in a blind hole in the bottom portion of the actuator block ([Figure 2B](#)). A compression spring was placed over the head of each leadscrew ([Figure 2C](#)), and the screw guide was fixed on top of the PCB ([Figure 2D](#)). When all the parts are assembled, the screw guide compresses the springs and forces contact between each leadscrew and the corresponding contact on the PCB. In this manner, a signal path is established between the electrode, shuttle, leadscrew, and PCB that does not require any loose wires ([Figures 1B and 1C](#)). The PCB routes the signals to eight 36-pin connectors (Omnetics). In the final step, the exposed electrodes ([Figure 2E](#)) were retracted so the tips lie 0.5 mm inside the distal opening of the guide tubes (design 1) or 1.5 mm inside the bottom of the guide array (design 2). The entire assembly was then gas sterilized before the sealing procedure.

The microdrives were sealed in several steps. In design 1, each guide tube was injected with sterile silicone oil (M1000,

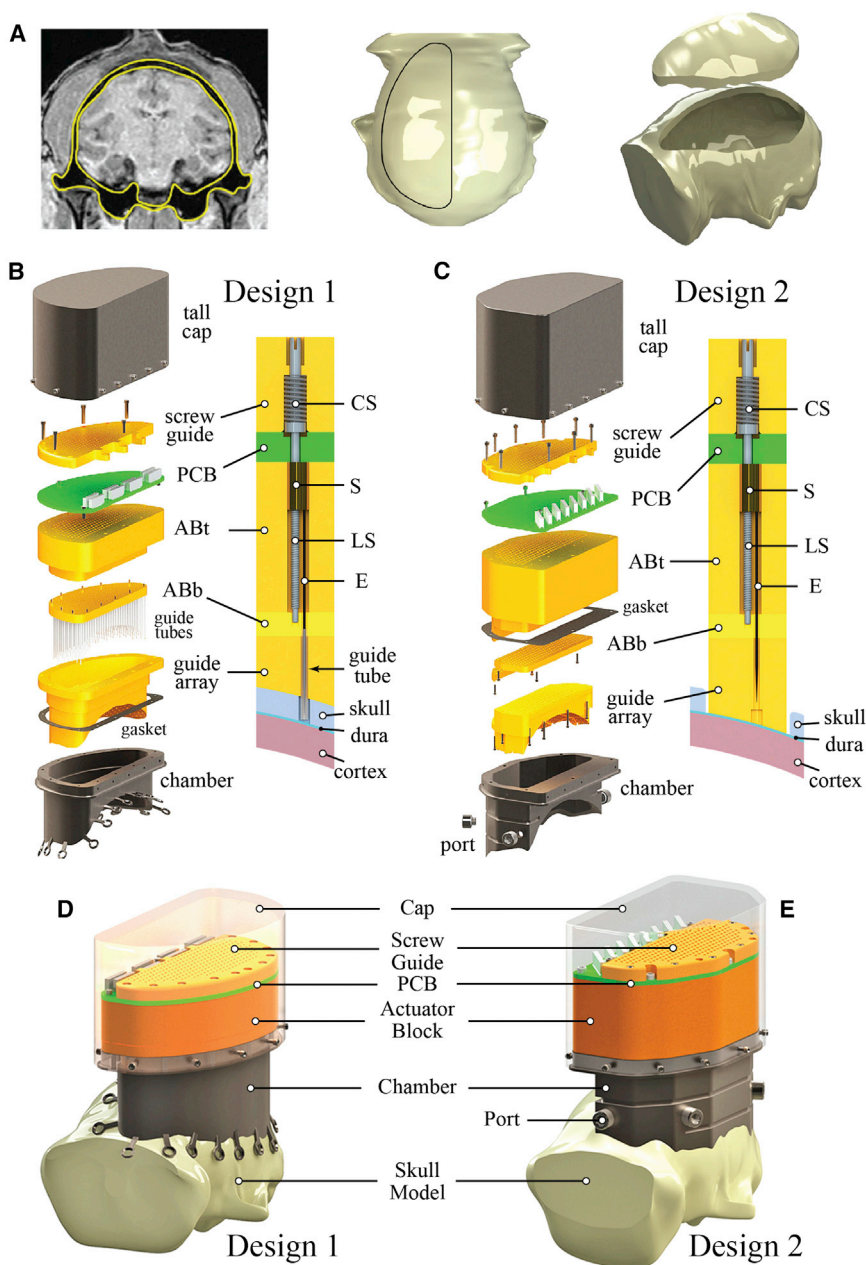


Figure 1. Design Drawings for Designs 1 and 2 of the Large-Scale Chamber and Microdrive System

(A) Illustration of the 3D skull model. A coronal section of the MRI is shown on the left with the inner and outer surfaces of the cranial bone outlined in yellow. The middle and right images show the skull model highlighting the boundaries of the intended craniotomy.

(B and C) Exploded views of the design drawings for design 1 (B) and design 2 (C) of the complete system. The insets show a cutaway view (not to scale) of the actuator mechanism.

(D and E) Assembled views of the design drawings for design 1 (D) and design 2 (E) mounted on their respective cranial models.

Abbreviations: PCB, printed circuit board; ABt, actuator block top; ABb, actuator block bottom; CS, compression spring; S, shuttle; LS, lead-screw; E, electrode.

Implanting the Chamber and Microdrive

We implanted the recording system in three stages—chamber implantation, craniotomy, and microdrive implantation—each followed by a period of recovery and testing to insure the health of the animals before proceeding to the next stage. All surgical and daily care, behavioral training, and animal handling procedures were performed in accordance with NIH guidelines and the Institutional Animal Care and Use Committee of Montana State University.

To implant the chamber, we successively retracted the skin, fascia, muscle, and periosteum from the cranial bone over an area slightly larger than the chamber. The chamber was placed in position and sealed around its perimeter with a thin bead of C&B-Metabond (Parkell) cement. It was then anchored to the skull using Titanium bone screws (Gray Matter Research) and acrylic bone cement. Design 1 incorporated legs that were

welded to the bottom surface of the chamber at ~ 1 cm intervals and included beveled holes for flathead bone screws (Figures 1B and 1D). The second design included a series of horizontal grooves around the perimeter of the chamber to allow bone cement to firmly anchor the chamber to a set of bone screws mounted around the perimeter (Figures 1C and 1E).

Thomas Recording) to act as a barrier to fluid flow (data not shown). In design 2, we took a different approach and injected each guide hole with a calibrated volume of sterile silicone grease (Figure 2F) (High-Vacuum Grease, Dow Corning), and the bottom surface of the guide array was painted with several uniform layers of sterile silicone sealant (Figure 2G) (734 Flowable Sealant, Dow Corning). The combination of techniques used in design 2 ensured that each guide hole was watertight, allowing for the downward movement of the electrode without any inward flow of fluid. Separate tests demonstrated that electrodes would easily pass through the silicone sealant without any changes in tip impedance.

After implanting the chamber, the cranial bone was left intact, and a silicone gasket and short plug were mounted on to the chamber and covered with a short protective cap (Figure S2A). The animals were given a minimum of 6 weeks to recover from this procedure before proceeding to the next stage. This allowed us to ensure that they were in good health and that the chamber

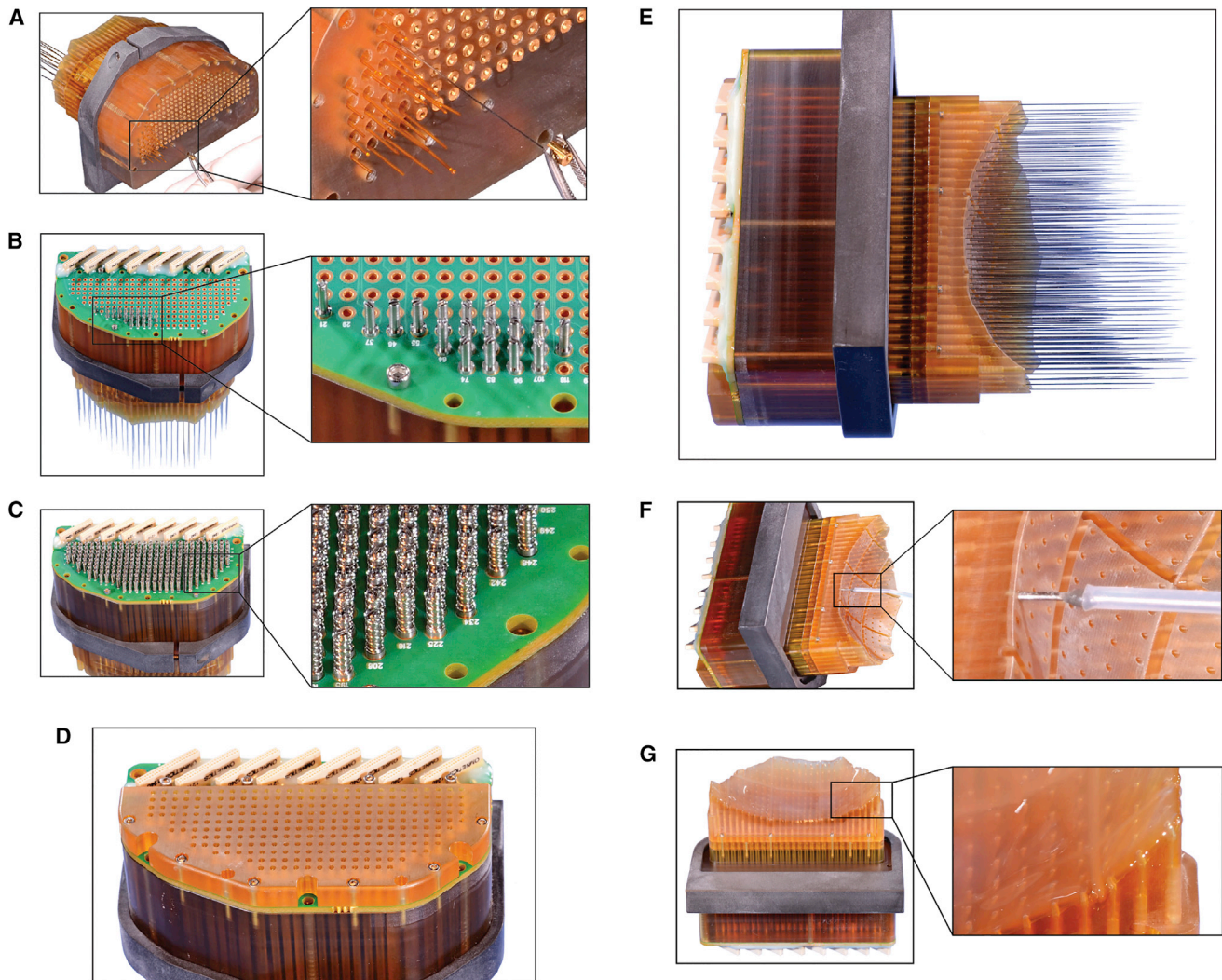


Figure 2. Steps in the Assembly and Sealing of the Microdrive System for Design 2 Only

(A) An oblique view of the partially assembled microdrive (top and bottom actuator blocks and guide array) mounted in a holder (gray) while an electrode is being front loaded into one of the polyimide tubes.

(B) Top-down view of the microdrive with the PCB mounted and a set of leadscrews inserted.

(C) The same view as in (B) with all of the leadscrews and compression springs loaded.

(D) Larger view of the microdrive with screw guide securely mounted.

(E) Side view of the assembled microdrive with all electrodes fully extended.

(F) Image showing how the sterile silicone grease is injected into each guide hole.

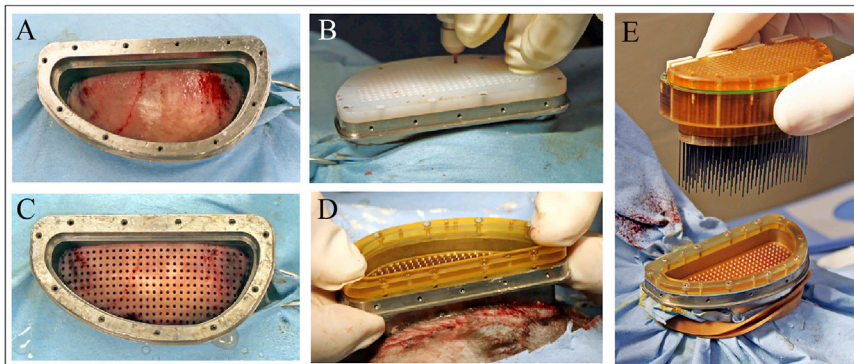
(G) Bottom-up view showing the layer of silicone sealant on the bottom surface of the guide array.

was well anchored and free of both external and internal infection.

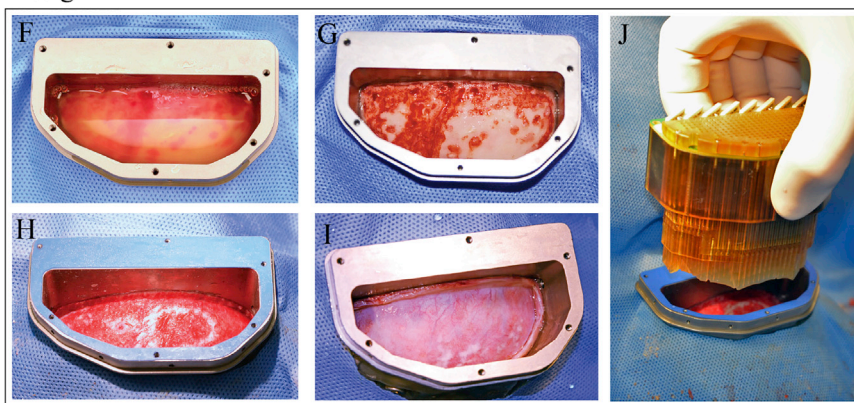
The second and third stages of implantation differed between the two designs. In the first design, we used stainless steel guide tubes (24G), press fit into the bottom of the actuator block, to protect the tip of each electrode (Figure 1B). The guide array was mounted within the chamber as a separate part and served to ensure that the array of guide tubes maintained accurate alignment (Figure 1B). The bottom surface of the guide array was offset from the top surface of the cranial bone by 1 mm to avoid mechanical contact. The guide tube lengths were adjusted

so that their distal ends extended into each cranial hole and came to rest just above the dura when the microdrive was mounted within the chamber (Figure 1B). A separate drill guide was constructed with the same shape as the guide array so that a hole could be accurately drilled into the cranial bone at the correct location for each electrode. Cranial holes were drilled (stage 2) and the microdrive was implanted (stage 3) in one sterile surgical procedure (Figures 3A–3E; Figure S2). After removing the cap, plug, and gasket, the chamber was rinsed and the cranial surface debrided of any connective tissue (Figure 3A). The drill guide was mounted onto the chamber, and 256 holes were

Design 1



Design 2

**Figure 3. Craniotomy and Microdrive Implantation Procedures for Stages II and III**

The images in (A)–(E) illustrate the implantation procedure for monkey 1 (design 1).

(A) View of the interior of the chamber following the aspiration of fluid and connective tissue.

(B) Drilling cranial holes using the drill guide (white).

(C) View of the chamber interior after drilling the cranial holes.

(D) Insertion of the guide array.

(E) Mounting of the microdrive.

The images in (F)–(J) show similar steps for monkey 2 (design 2).

(F) View of the chamber interior 6 weeks after implantation. Accumulated fluid is visible.

(G) Same view after aspiration of the fluid.

(H) Chamber interior immediately following the craniotomy.

(I) Chamber interior 12 weeks after the craniotomy. The dural membrane is healthy and shows signs of growth around the perimeter of the form-fitting plug.

(J) Mounting of the microdrive (note: this image shows a test of the microdrive fit immediately after the craniotomy was made, not the actual implantation, which was done 12 weeks later.).

drilled through the cranial bone using a hand-held motorized drill (Figure 3B). After removing the guide, the bone was rinsed until all bleeding had ceased, and the gasket, guide array, and microdrive were installed and fixed to the chamber with machine screws (Figures 3C–3E).

In the second design, the guide array was constructed to conform to the inner surface of the skull and was anchored to the actuator block with machine screws (Figure 1C). Each hole in the guide array served to support and guide each electrode as it passed through the exposed dura and into the brain. For the second design, we separated the craniotomy procedure (stage 2) from the microdrive implantation (stage 3) (Figure S2). Approximately 6 weeks after the chamber implant, we performed a craniotomy within the interior of the chamber while leaving the dural membrane intact (Figures 3F–3H). A Kerrison Rongeur was used to avoid damage to the dura and ensure an accurate opening in the bone. The chamber was sealed with a gasket and a form-fitting plug that was contoured to the internal cranial surface (Figure S2). This re-sealed the cranial cavity and prevented herniation. The animal was given 12 weeks to recover from the procedure. During this time, we continually assessed the health of the animal and cultured the fluid inside the chamber at 3-week intervals using one of the drainage ports to gain access. Each of these tests was negative for infection, allowing us to proceed to the final stage with some assurance of the sterility of the chamber. In this procedure, the form-fitting plug was removed, the

chamber interior was cleaned of connective tissue, and the assembled microdrive mounted after replacing the silicone gasket (Figures 3I and 3J). The microdrive was secured with machine screws passing through the actuator block to the chamber. For both designs, the assemblies were covered with a protective aluminum cap following the microdrive implantation (Figures 1D and 1E).

In both experiments, once the microdrive was mounted, it remained on the animal for the duration of the experiment (6 months in monkey 1, 9 months in monkey 2). The chamber served as the reference and ground connection to the animal using a machine screw linked to a trace on the PCB.

Large-Scale Recordings in Behaving Non-human Primates

We trained both monkeys to perform an object-based dMTS and a passive fixation task. Once the monkeys reached criterion performance on the dMTS task (>85% correct), we carried out the implantation sequence and began neural recordings when the animals were fully recovered, healthy, and performing the task normally. To initiate recordings, we gradually moved all the electrodes through the dura and into the cortex over a period of 2–4 weeks. This was done in an incremental manner by advancing a subset of 10–30 electrodes each day until unit activity was detected. During this process, we routinely measured electrode impedance and ceased advancing an electrode whenever its impedance was less than ~50 k Ω or more than ~2.5 M Ω . We considered low-impedance electrodes to have damaged tips and did not move them further. We attempted to adjust the high-impedance electrodes and recover the signal. If this failed, we

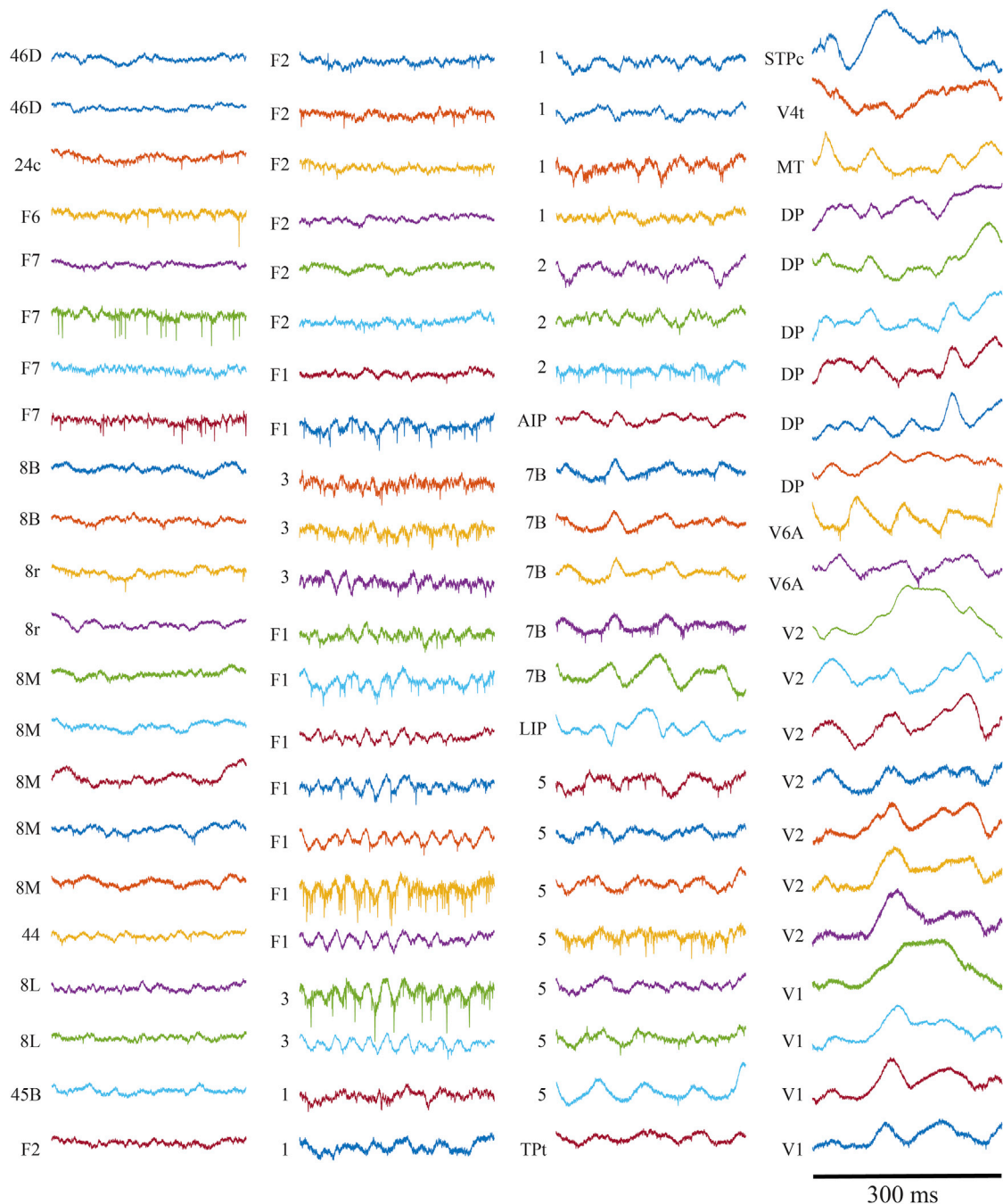


Figure 4. A Brief 300 ms Segment of Broadband Data Simultaneously Sampled from 88 Microelectrodes in Monkey 2 Just Prior to the Onset of the Match Stimulus during the dMTS Task

The cortical area of each recording is indicated just to the left of each trace according to the nomenclature of [Markov et al. \(2014\)](#).

considered the actuator or electrode to be damaged and did not move these electrodes further.

Once we identified all of the functioning electrodes, we carried out daily recording sessions 3–5 days/week over a period of 6 and 9 months in monkeys 1 and 2, respectively. A total of 25 and 62 recording sessions were selected for further analysis for monkey 1 and monkey 2, respectively. Sessions were

excluded for various reasons common to electrophysiological experiments such as the animal's behavioral performance, the running of separate tasks, or technical issues with the recording and task presentation hardware/software. [Figure 4](#) shows an example of the broadband signals simultaneously recorded from 88 selected example electrodes in monkey 2 ([Figure S4](#) shows the data obtained for the entire trial.). When moving the

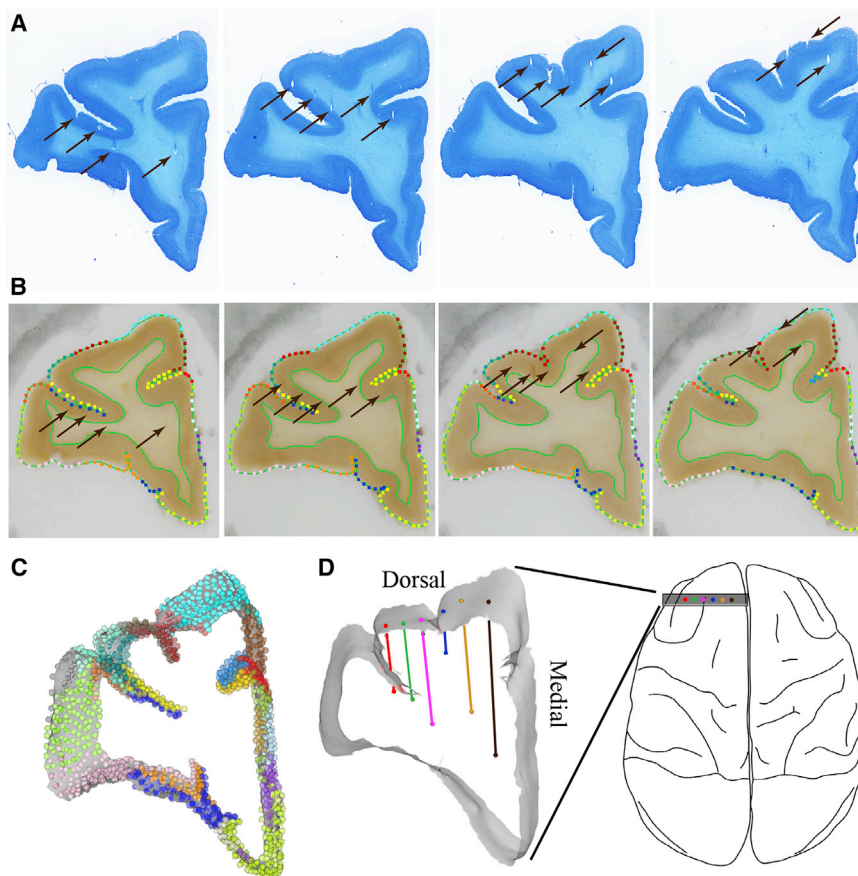


Figure 5. Anatomical Reconstruction Process

(A) Nissl-stained sections of prefrontal cortex. Arrows indicate lesions or small holes made by the electrodes.

(B) Photographs of the face of the frozen tissue block during sectioning aligned to the histological sections in (A). The arrows correspond to those shown in (A). The dotted lines mark the outer cortical surface, where each distinct color marks a different cortical area according to the atlas of Markov et al. (2014). The solid green lines mark the inner cortical surface.

(C) A portion of prefrontal cortex reconstructed using the Caret software. Colored dots indicate cortical areas.

(D) Example of the reconstructed electrode tracts using the information from (A)–(C).

electrodes, our objective was to maximize the number of channels with detectable unit activity. However, we quickly discovered that it was too time consuming to search for unit activity on all channels each day. So at the beginning of each session, we inspected the signals and chose a subset of electrodes (ranging from 5 to 60) for further movement. We advanced these electrodes in increments of one-quarter to 1 turn of the lead-screw (~ 30 – $120 \mu\text{m}$) and typically did not advance any electrode more than 1 mm on any given day.

For subsequent analysis of the data, it was important to know the anatomical location of each recording site over the course of both experiments. We therefore chose to end the recording phase of the experiments and proceed with the anatomical reconstructions. Here we describe the technique for monkey 2; the technique for monkey 1 is provided in the STAR Methods. To estimate the location of each recording site, we combined several sources of information using the Computerized Anatomical Reconstruction and Editing Toolkit (Caret) (Van Essen, 2012). During the experiment, we kept a careful record of the depth of each recording site by counting the number of rotations of the leadscrew on each actuator. Once all recordings were completed, we made a small electrolytic lesion on each functioning electrode ($10 \mu\text{A}$ DC for 25 s) and then euthanized and perfused the animal with fixative with the microdrive in place and the electrodes extended to their final positions. We then removed the microdrive and later measured the distance that

each electrode extended beyond the bottom surface of the microdrive in order to compare with the experimental depth measurements. The snug fit between the lower portion of the microdrive and the inner wall of the chamber kept off-axis movements to a minimum. We then removed and photographed the recorded hemisphere and prepared it for histology. Frozen sections were cut in the coronal plane ($60 \mu\text{m}$ thickness) and every fifth section was stained for Nissl substance and photographed (FD Neurotechnologies).

During sectioning, we also photographed the frozen block face of the brain to accurately record the shape of each slice. Figure 5A shows four examples of the Nissl-stained sections obtained from prefrontal cortex. The arrows mark the locations of identified electrode tracks or lesions. We imported the block-face photographs into Caret and then traced the outer cortical surface and marked the location of each electrode track or lesion from the corresponding Nissl-stained section (Figure 5B). Using this information, the entire hemisphere was parsed into cortical areas based on the atlas reported in Markov et al. (2014) (Figure 5C). Then, using the identified electrode tracks and lesions from the histology, we reconstructed each electrode track over the entire hemisphere and assigned a cortical area to each recording site in the entire dataset (Figure 5D). This process was facilitated by the fact that the absence of unit data often corresponded with the electrode being positioned in white matter.

Following complete reconstruction of both datasets, we determined the total number of areas from which we recorded as well as the number of areas in which we made simultaneous measurements. We excluded all measurements in which there was no detectable unit activity. In monkey 1, we sampled neuronal activity from 114 different electrodes spanning a period of 155 days. These data included recordings from 37 different cortical areas with a maximum of 21 cortical areas measured simultaneously. In monkey 2, we recorded neuronal activity from 143 different electrodes spanning a period of 260 days.

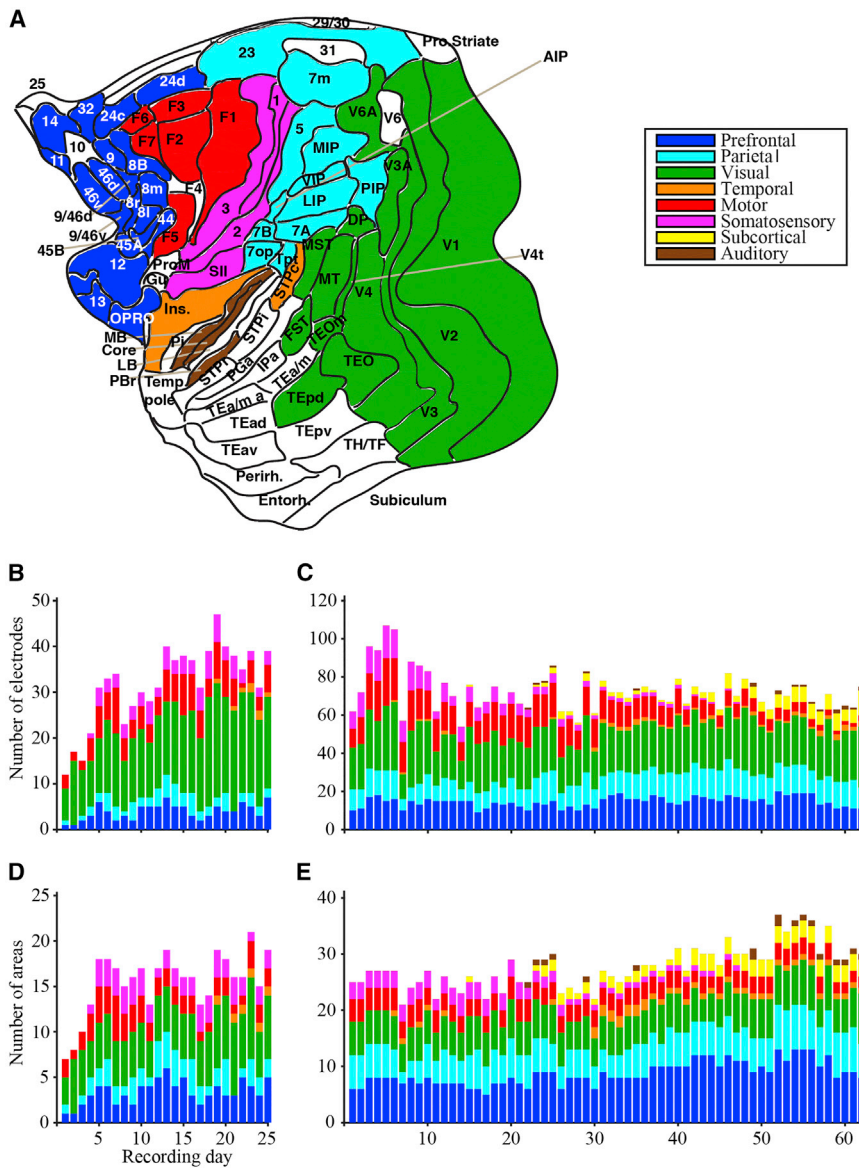


Figure 6. Summary of Recording Performance

(A) Flat map of the cortex taken from Markov et al. (2014) showing the cortical areas in which signals were recorded in both monkeys.

(B and C) Number of electrodes with detectable unit activity on each recording session for monkeys 1 (B) and 2 (C), respectively.

(D and E) Number of cortical areas (and subcortical nuclei) simultaneously sampled on each recording session for monkeys 1 (D) and 2 (E), respectively. In all plots, the colors indicate brain region (see legend).

detectable unit activity remained fairly stable (Figures 6B and 6C), but the composition of recorded cortical areas changed over time—especially in monkey 2 (Figures 6C and 6E). As electrodes were advanced, some of them passed from gray matter into white matter, causing them to be excluded from the sample, while others followed the opposite pattern. Similarly, over time, there was a reduction in measurements of motor and somatosensory areas accompanied by an increase in recordings from subcortical nuclei (especially in monkey 2). In general, the recording quality remained stable throughout the entire experiment, and the electrodes displayed both increases and decreases in impedance over time (Figure S5).

Segregated Functional Networks Revealed by Relative Phase Relationships

To demonstrate the power of this technique for understanding large-scale neuronal circuits, we used graph theoretic tools to study functional connectivity networks during the working memory

Data were collected from 56 separate cortical areas and 4 subcortical nuclei (caudate, putamen, thalamus, and claustrum). The maximum number of cortical areas recorded simultaneously in monkey 2 was 37. Combining the results from both experiments, we made recordings from a total of 61 cortical areas and 4 subcortical nuclei (Figure 6A). These data yielded a total of 335 well-isolated single-unit recordings and 5,365 multi-unit recordings. In each of these recordings, we also recovered the local field potential (LFP) signal.

Next, we wanted to know how the system performed over time. Figures 6B and 6C show the number of electrodes with detectable unit activity during each recording session, and Figures 6D and 6E show the number of cortical/subcortical areas in which these signals were measured simultaneously during each recording session. Over time, as we slowly advanced the electrodes through the tissue, the number of electrodes with

task. The relative phase of the oscillatory activity between separate neural populations provides a candidate mechanism for modulating the integration/segregation of functional networks (Dotson et al., 2014; Maris et al., 2016). We have previously shown that the relative phase relationships between LFPs in widely separated cortical areas in the frontoparietal network are highly dynamic and concentrated near 0° (in-phase) or 180° (anti-phase) in the beta frequency band (12–25 Hz) (Dotson et al., 2014; Dotson and Gray, 2016). This finding suggests that anti-phase synchronization could be a mechanism for segregating functional networks. However, we know nearly nothing about the large-scale spatial distribution of phase relationships or their function. We addressed this issue by asking how the modularity of functional connectivity networks, computed using phase locking analysis, is modified when relative-phase information is taken into account.

We performed a phase-locking analysis of the LFP signals at multiple narrow bands to quantify the phase-locking value (PLV) and its relative phase angle for each pair of signals as a function of frequency. These data were then used to create the functional connectivity networks. The phase-locking analysis was performed following Tass et al. (1998), and we assessed the statistical significance of each PLV by comparing the observed PLV to surrogate distributions (see STAR Methods for more details). This analysis was performed on a recording session from monkey 2. We used a 400 ms window during the delay period, starting 400 ms after the sample offset. We first wanted to know if the relative phase angles were bimodally distributed, similar to what we observed in the frontoparietal network (Dotson et al., 2014). Figure 7A shows that the relative phase distributions for three frequency bands (6–9 Hz, 12–21 Hz, and 24–30 Hz) during the delay period of the dMTS task are indeed bimodal.

Based on the assumption that anti-phase links serve to functionally segregate networks, we wanted to know how removing the anti-phase links affected the community structure of the functional connectivity network. To accomplish this, we used a graph theoretic measure called modularity, which determines the community structure of a network by dividing the network in a way that maximizes the within-community links and minimizes the between-community links (Rubinov and Sporns, 2010). Networks with a high modularity display largely non-overlapping communities. We used the phase-locking data in the 12–21 Hz band to create functional connectivity networks for the full network (both in-phase and anti-phase links) and the in-phase-only network. The anti-phase only network was too sparse to be considered. We chose to focus on the 12–21 Hz band due to its relevance to working memory (Salazar et al., 2012; Dotson et al., 2014). We calculated the modularity for the full network and the in-phase-only network using nine different PLV thresholds. Multiple thresholds were used to enable the exploration of high-density and low-density networks, ensuring that our results are not a result of a specific threshold (Bassett et al., 2008; Bullmore and Bassett, 2011; Power et al., 2011). The light blue line and black line in Figure 7B show the modularity values for the full network and in-phase-only network at each PLV threshold, respectively. This revealed that the modularity of the in-phase-only network is well above the full network at all thresholds. Since simply removing links will result in an increase in modularity, we created a population of surrogate networks (both in-phase and anti-phase links) with the same number of links as the in-phase-only network. We have previously reported that anti-phase links are predominately inter-areal (Dotson et al., 2014), so we created the surrogate networks by kicking out a set of randomly selected inter-areal links from the full network. We show the mean \pm 3 SD of the surrogate distributions (solid and dashed red lines) in Figure 7B. This shows that the in-phase-only network is much more modular than the surrogate networks ($p < 0.01$ at all thresholds), indicating that the increase in modularity is due to exclusion of the anti-phase links.

In order to visualize these networks, we imported the functional connectivity networks into the software package Gephi and used a built in graph layout algorithm (Bastian et al., 2009; Jacomy et al., 2014). Figure 7C shows the full network, with

dot colors coded by modules (12–21 Hz; PLV threshold = 0.015). We see that there are four modules distributed across the recording sites (inset). In Figure 7D, we see that after removing the anti-phase links, the visual module (orange) is entirely separated from the other modules, indicating that the visual module is linked to the parietal, frontal, and prefrontal areas with anti-phase links. There is also an additional module revealed. The green module covering part of the posterior parietal cortex in Figure 7C appears to be split across the intra-parietal sulcus (IPS) in Figure 7D, similar to Dotson et al. (2014), where the signals on opposite sides of the IPS were shown to be anti-phase.

DISCUSSION

We have developed and implemented a large-scale, semi-chronic chamber and microdrive system that enables long-term recordings of neuronal activity from large numbers of independently movable microelectrodes spanning the depth and breadth of one hemisphere of the brain in behaving non-human primates. This approach provides an unprecedented advance in the ability of researchers to measure and characterize the dynamics of large-scale neural circuit activity and its relation to behavior. It greatly expands the area over which simultaneous measurements can be made and allows the targeting of specific, but widely distributed, neural circuits. By enabling the independent control of electrode position, the approach circumvents the limitations of chronically implanted fixed recording arrays and greatly expands the number of electrodes that can be implanted with acute recording techniques. Because the electrodes remain implanted for long periods, the time required to set up and take down an experiment are reduced to minutes rather than hours.

This method has the potential to open up new realms of investigation. It is becoming increasingly evident that the relative phase relationships within and between cortical areas may function to both integrate and segregate cortical networks (Dotson et al., 2014; Maris et al., 2016). We demonstrate, as a “proof of principle,” the ability to address network-level questions that incorporate relative phase relationships in the LFP signals, which is difficult to do with other large-scale recording methods such as magnetoencephalography (MEG) and electrocorticography (ECoG). We are able to characterize the large-scale structure of functional networks and find that excluding the anti-phase links leads to a jump in the modularity of the network. This change is larger than one would expect by simply removing the same number of randomly selected inter-areal links, and the result indicates that anti-phase links are not randomly distributed among cortical areas; rather, they selectively segregate certain cortical areas from one another.

Methodological Considerations

Several aspects of the design and approach pose significant challenges. First, the method relies on a wide array of technology, including structural magnetic resonance imaging, computer-aided design software, multi-axis computer numerical control (CNC) machining, and Swiss screw machine technology capable of making the exceptionally long, fine-gauge leadscrews. These

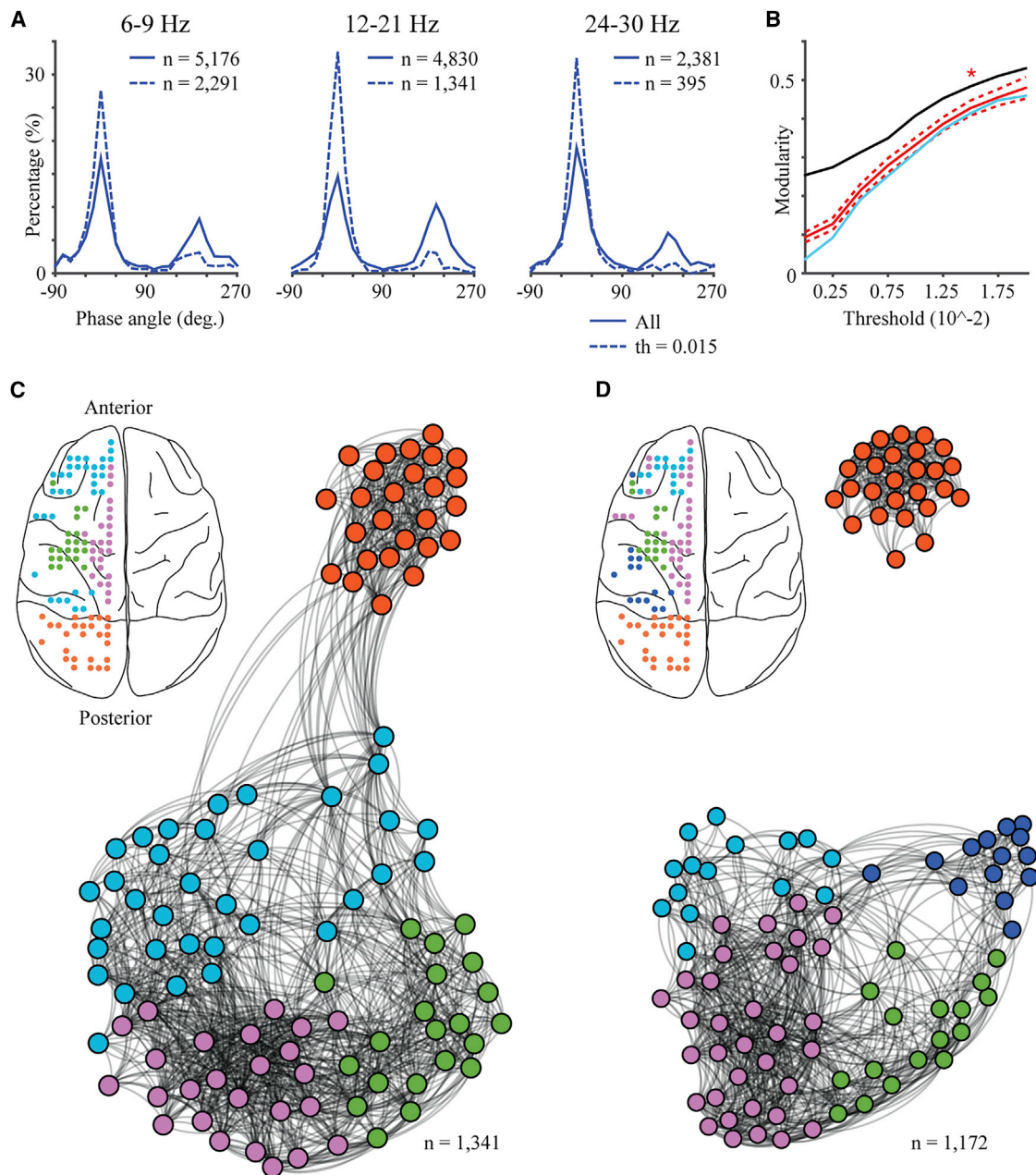


Figure 7. Results of the Functional Connectivity Analysis

(A) Histograms of the relative phase distributions for three frequency bands in the LFP during the delay period of the task. The solid and dashed lines show all the statistically significant values (see STAR Methods) and those that exceeded a PLV magnitude of 0.015, respectively.

(B) Modularity as a function of the PLV magnitude threshold. The light blue line shows the modularity value for the network with all links (full network). The black line is the modularity value for the in-phase-only network. The solid and dashed red lines show the mean \pm 3 SD of the surrogate distributions. The red asterisk indicates the PLV threshold value (0.015) used for the visualization shown in (C) and (D).

(C and D) Visualization of the cortical network with all links (C) and with only in-phase links (D). Colors indicate modules. Inset brain images show the corresponding locations of electrode entry into the brain.

technologies can be expensive and are not always routinely available. For these reasons, we contracted much of the machining and manufacture of the precision components.

Second, the assembly and loading of the microdrive system requires a high degree of patience, manual dexterity, and atten-

tion to detail. All of the components must be assembled using sterile technique and great care must be taken to ensure that all avenues for the entry of fluid into the system are sealed.

Third, the surgical procedures for implanting the chamber, performing the craniotomy, and maintaining the good health of

the animal also pose a number of challenges. The chamber system must be held rigidly to the cranial bone with a large number of bone screws linked with bone cement to the external chamber wall, and it's necessary to establish a watertight seal at the interface between the cranial bone and the bone cement. Flaws in either of these procedures can lead to infection within the chamber or subsequent mechanical failure of the implant. The skin surrounding the implant must be carefully sutured to avoid gaps that can lead to external infection, inflammation, and discomfort for the animal. Both methods that we employed for gaining access to the brain—the drilling of hundreds of individual holes or performing a hemispherical craniotomy—required great care and attention. We found the latter approach to be preferable because it eliminated the risk of damaging the underlying dura when using a high-speed drill without visual guidance.

Fourth, the passage of large numbers of semi-chronically implanted microelectrodes through the dura can lead to leakage of cerebrospinal fluid (CSF) into the epidural space. If this fluid accumulates, it can lead to an increase in pressure and potential compression of the brain. While we designed the ports in the chamber wall to enable the sampling, and subsequent culturing, of fluid from inside the chamber (design 2), it proved difficult to use the same ports to remove accumulated fluid during the recording phase of the experiment. However, this is an important concern, and future versions of the system could be designed to enable the removal of fluid and to provide the ability to flush the epidural space in the event of an infection.

Finally, we were unable to identify the anatomical locations of the recording sites when the experiment was in progress and had to wait for the histological reconstruction to obtain this valuable data. This is a significant issue because it requires the sacrifice of the animals and many months to complete the reconstruction and severely constrains the timely reporting of research findings. A simple solution to this problem is to fabricate as many of the components of the system as possible out of MRI-compatible plastic, such as ULTEM, PEEK, or 3D-printed materials. During various stages of the experiment, the animals could be re-scanned with fiducial markers mounted to the hardware and the electrode tip positions reconstructed on the basis of the scan and the recorded depths.

Overall Performance

Overall, the animals tolerated the implants quite well. Both animals quickly learned to avoid bumping the protective cap against the walls of their home cage, and the hardware remained stable for the duration of both experiments. We took great care to maintain the cleanliness of the wound margins around the perimeter of the implant. The first animal showed some bone decay within the chamber, which we attributed to compromised circulation within the bone due to the large number of cranial holes. On the second animal, we repeatedly tested the fluid within the chamber prior to implantation of the microdrive and found no indication of infection. At the end of the experiment, we removed the microdrive and found the residual fluid to be clear, with no sign of infection. Moreover, we found that the bone regrew a thin membrane around the inside perimeter

of the chamber, which did not encroach on the recording electrodes.

While the recordings were generally quite stable and displayed excellent signal-to-noise ratio, several factors led to reduced yields in the sampling of neuronal activity. In the first animal, a substantial number of channels were lost when fluid entered a small number of guide tubes and traveled back up to the PCB and short-circuited a number of channels. We solved this problem in the second experiment by back filling each guide hole with sterile silicone grease and sealing the bottom surface with a silicone sealant. Another problem occurred when rotation of the leadscrew led to some rotation of the shuttle. This caused the electrode to bend, which affected the recording quality and occasionally led to breakage of the glass insulation on the electrode and failure of that channel. We attributed this problem to variance in the internal diameter of the guide hole within the actuator block, allowing the shuttle to rotate as the leadscrew was rotated over part of the travel distance. Another problem, largely out of our control, occurred when the delicate electrode tips changed impedance or broke when passing through the dural membrane. Finally, over the course of both experiments each electrode passed through substantial sections of white matter, preventing us from recording neuronal activity. In spite of these combined factors, we were nonetheless able to sample neuronal activity from a large number of cortical sites spanning a large fraction of the cortical mantle.

Future Directions

Since completing this study, we have made a number of improvements in the design of the system. To prevent rotation of the shuttles when advancing the electrodes, we designed a shuttle with a teardrop cross-sectional shape and utilized 3D printing technology to fabricate the actuator block with matching teardrop shaped channels (A.B. Goodell and C.M. Gray, 2015, Soc. Neurosci., abstract). This greatly increased the reliability of the actuators, increased the efficiency of fabrication of the actuator block, and enabled us to modify the exit path of the guide holes so that the inter-electrode spacing could be decreased. We have improved the design of the leadscrews to provide up to 42 mm of electrode travel with a thread pitch of 8 turns/mm and modified the design of the screw head and screwdriver to a half-moon shape. These changes have enabled the device to target structures on the ventral surface of the brain and enhanced the screwdriver-lead-screw interface.

Several further design changes could greatly enhance the performance of the system and the ease with which it is implanted and maintained. First, control of each actuator could be automated. This would require the design of a robotic screwdriver capable of indexing each channel in the array, delivering a specified change in electrode depth, and tracking all of the information in conjunction with data acquisition. Second, the recording yield of the system could be increased by an order of magnitude by introducing multi-contact silicon polytrodes. Such probes would likely require long, flexible ribbon cables to tether the signals to a set of electrode interface boards or active on-board electronics for digitizing and multiplexing the large numbers of signals. This would require a change to the design of the actuator

mechanism and the incorporation of probes with sufficient rigidity to pass through the dura unaffected. Finally, the future implementation of this large-scale approach would benefit greatly from a design that minimizes the number of surgical procedures and eliminates the need for acrylic bone cement. We think this could be accomplished by designing a prosthetic platform that conforms to each animal's cranial surface and could be mounted in a single surgical procedure without the use of acrylic bone cement (Mulliken et al., 2015). The device would include prefabricated ports, in which a craniotomy could be made and specialized microdrives implanted for recording and manipulating neuronal activity in large-scale circuits.

STAR★METHODS

Detailed methods are provided in the online version of this paper and include the following:

- [KEY RESOURCES TABLE](#)
- [CONTACT FOR REAGENT AND RESOURCE SHARING](#)
- [EXPERIMENTAL MODEL AND SUBJECT DETAILS](#)
 - Subjects
- [METHOD DETAILS](#)
 - Behavioral Task
 - Chamber System
 - Electrophysiological Recordings
 - Anatomical Reconstruction Technique for Monkey 1
- [QUANTIFICATION AND STATISTICAL ANALYSIS](#)
 - Network Analysis

SUPPLEMENTAL INFORMATION

Supplemental Information includes five figures and can be found with this article online at <https://doi.org/10.1016/j.neuron.2017.09.050>.

AUTHOR CONTRIBUTIONS

C.M.G. and B.G. conceived and designed the recording system. N.M.D. and C.M.G. designed the experiments. C.M.G. and N.M.D. performed the surgical procedures. N.M.D., S.J.H., and C.M.G. tested the recording system and implemented design modifications, performed the experiments, processed and analyzed the data, and wrote the paper. B.G. assisted with all design and fabrication aspects of the project.

ACKNOWLEDGMENTS

We are grateful to Dr. Chris O'Rourke for her excellent care of the animals and assistance in this study. We thank Tiphani Lynn for her help with the histological parcellation of cortical areas. We thank Elliot Gray for his expert assistance in the assembly and testing of the microdrives. We thank Susan Krueger for her help in the behavioral training and daily care of the animals. We also thank Neuralynx (Neuralynx, Bozeman MT, USA) for providing the data acquisition system. This work was supported by grants from NINDS (R01 NS059312), NIMH (R01 MH081162), and the McKnight Foundation Memory and Cognitive Disorders Award to C.M.G. All data are stored at Montana State University and are available on request.

Received: May 19, 2017

Revised: August 8, 2017

Accepted: September 26, 2017

Published: October 26, 2017

REFERENCES

- Andrey, P., and Maurin, Y. (2005). Free-D: an integrated environment for three-dimensional reconstruction from serial sections. *J. Neurosci. Methods* *145*, 233–244.
- Antzoulatos, E.G., and Miller, E.K. (2014). Increases in functional connectivity between prefrontal cortex and striatum during category learning. *Neuron* *83*, 216–225.
- Asaad, W.F., and Eskandar, E.N. (2008a). Achieving behavioral control with millisecond resolution in a high-level programming environment. *J. Neurosci. Methods* *173*, 235–240.
- Asaad, W.F., and Eskandar, E.N. (2008b). A flexible software tool for temporally-precise behavioral control in Matlab. *J. Neurosci. Methods* *174*, 245–258.
- Asaad, W.F., Rainer, G., and Miller, E.K. (2000). Task-specific neural activity in the primate prefrontal cortex. *J. Neurophysiol.* *84*, 451–459.
- Bassett, D.S., Bullmore, E., Verchinski, B.A., Mattay, V.S., Weinberger, D.R., and Meyer-Lindenberg, A. (2008). Hierarchical organization of human cortical networks in health and schizophrenia. *J. Neurosci.* *28*, 9239–9248.
- Bastian, M., Heymann, S., and Jacomy, M. (2009). Gephi: an open source software for exploring and manipulating networks. *ICWSM* *8*, 361–362.
- Battaglia, F.P., Kalenscher, T., Cabral, H., Winkel, J., Bos, J., Manuputy, R., van Lieshout, T., Pinkse, F., Beukers, H., and Pennartz, C. (2009). The Lantern: an ultra-light micro-drive for multi-tetrode recordings in mice and other small animals. *J. Neurosci. Methods* *178*, 291–300.
- Bullmore, E.T., and Bassett, D.S. (2011). Brain graphs: graphical models of the human brain connectome. *Annu. Rev. Clin. Psychol.* *7*, 113–140.
- Buschman, T.J., and Miller, E.K. (2007). Top-down versus bottom-up control of attention in the prefrontal and posterior parietal cortices. *Science* *315*, 1860–1862.
- Csicsvari, J., Henze, D.A., Jamieson, B., Harris, K.D., Sirota, A., Barthó, P., Wise, K.D., and Buzsáki, G. (2003). Massively parallel recording of unit and local field potentials with silicon-based electrodes. *J. Neurophysiol.* *90*, 1314–1323.
- deCharms, R.C., Blake, D.T., and Merzenich, M.M. (1999). A multielectrode implant device for the cerebral cortex. *J. Neurosci. Methods* *93*, 27–35.
- Dickey, A.S., Suminski, A., Amit, Y., and Hatsopoulos, N.G. (2009). Single-unit stability using chronically implanted multielectrode arrays. *J. Neurophysiol.* *102*, 1331–1339.
- Donoghue, J.P., Sanes, J.N., Hatsopoulos, N.G., and Gaál, G. (1998). Neural discharge and local field potential oscillations in primate motor cortex during voluntary movements. *J. Neurophysiol.* *79*, 159–173.
- Dotson, N.M., and Gray, C.M. (2016). Experimental observation of phase-flip transitions in the brain. *Phys. Rev. E Stat. Nonlin. Soft Matter Phys.* *94*, 042420.
- Dotson, N.M., Salazar, R.F., and Gray, C.M. (2014). Frontoparietal correlation dynamics reveal interplay between integration and segregation during visual working memory. *J. Neurosci.* *34*, 13600–13613.
- Dotson, N.M., Goodell, B., Salazar, R.F., Hoffman, S.J., and Gray, C.M. (2015). Methods, caveats and the future of large-scale microelectrode recordings in the non-human primate. *Front. Syst. Neurosci.* *9*, 149–149.
- Eliades, S.J., and Wang, X. (2008). Chronic multi-electrode neural recording in free-roaming monkeys. *J. Neurosci. Methods* *172*, 201–214.
- Erickson, C.A., and Desimone, R. (1999). Responses of macaque perirhinal neurons during and after visual stimulus association learning. *J. Neurosci.* *19*, 10404–10416.
- Fee, M.S., and Leonardo, A. (2001). Miniature motorized microdrive and commutator system for chronic neural recording in small animals. *J. Neurosci. Methods* *112*, 83–94.

- Feingold, J., Desrochers, T.M., Fujii, N., Harlan, R., Tierney, P.L., Shimazu, H., Amemori, K., and Graybiel, A.M. (2012). A system for recording neural activity chronically and simultaneously from multiple cortical and subcortical regions in nonhuman primates. *J. Neurophysiol.* *107*, 1979–1995.
- Fries, P., Roelfsema, P.R., Engel, A.K., König, P., and Singer, W. (1997). Synchronization of oscillatory responses in visual cortex correlates with perception in interocular rivalry. *Proc. Natl. Acad. Sci. USA* *94*, 12699–12704.
- Gray, C.M., and Goodell, B. (2011). Spatiotemporal dynamics of synchronous activity across multiple areas of the visual cortex in the alert monkey. In *The Dynamic Brain: An Exploration of Neuronal Variability and Its Functional Significance*, M. Ding and D. Glanzman, eds. (Oxford University Press), pp. 233–254.
- Gray, C.M., Goodell, B., and Lear, A. (2007). Multichannel micromanipulator and chamber system for recording multineuronal activity in alert, non-human primates. *J. Neurophysiol.* *98*, 527–536.
- Hernández, A., Nacher, V., Luna, R., Alvarez, M., Zainos, A., Cordero, S., Camarillo, L., Vázquez, Y., Lemus, L., and Romo, R. (2008). Procedure for recording the simultaneous activity of single neurons distributed across cortical areas during sensory discrimination. *Proc. Natl. Acad. Sci. USA* *105*, 16785–16790.
- Hoffman, K.L., and McNaughton, B.L. (2002). Coordinated reactivation of distributed memory traces in primate neocortex. *Science* *297*, 2070–2073.
- Jacomy, M., Venturini, T., Heymann, S., and Bastian, M. (2014). ForceAtlas2, a continuous graph layout algorithm for handy network visualization designed for the Gephi software. *PLoS ONE* *9*, e98679.
- Kim, T., Troyk, P.R., and Bak, M. (2006). Active floating micro electrode arrays (AFMA). In *28th Annual International Conference of the IEEE (Engineering in Medicine and Biology Society)*, pp. 2807–2810.
- Kipke, D.R., Vetter, R.J., Williams, J.C., and Hetke, J.F. (2003). Silicon-substrate intracortical microelectrode arrays for long-term recording of neuronal spike activity in cerebral cortex. *IEEE Trans. Neural Syst. Rehabil. Eng.* *11*, 151–155.
- Kloosterman, F., Davidson, T.J., Gomperts, S.N., Layton, S.P., Hale, G., Nguyen, D.P., and Wilson, M.A. (2009). Micro-drive array for chronic in vivo recording: drive fabrication. *J. Vis. Exp.* (26), 1094, <https://doi.org/10.3791/1094>.
- Krupa, D.J., Wiest, M.C., Shuler, M.G., Laubach, M., and Nicolelis, M.A. (2004). Layer-specific somatosensory cortical activation during active tactile discrimination. *Science* *304*, 1989–1992.
- Maris, E., Fries, P., and van Ede, F. (2016). Diverse phase relations among neuronal rhythms and their potential function. *Trends Neurosci.* *39*, 86–99.
- Markov, N.T., Ercsey-Ravasz, M.M., Ribeiro Gomes, A.R., Lamy, C., Magrou, L., Vezoli, J., Misery, P., Falchier, A., Quilodran, R., Gariel, M.A., et al. (2014). A weighted and directed interareal connectivity matrix for macaque cerebral cortex. *Cereb. Cortex* *24*, 17–36.
- Markowitz, D.A., Wong, Y.T., Gray, C.M., and Pesaran, B. (2011). Optimizing the decoding of movement goals from local field potentials in macaque cortex. *J. Neurosci.* *31*, 18412–18422.
- Maynard, E.M., Hatsopoulos, N.G., Ojakangas, C.L., Acuna, B.D., Sanes, J.N., Normann, R.A., and Donoghue, J.P. (1999). Neuronal interactions improve cortical population coding of movement direction. *J. Neurosci.* *19*, 8083–8093.
- Mendoza, G., Peyrache, A., Gámez, J., Prado, L., Buzsáki, G., and Merchant, H. (2016). Recording extracellular neural activity in the behaving monkey using a semichronic and high-density electrode system. *J. Neurophysiol.* *116*, 563–574.
- Miller, E.K., and Wilson, M.A. (2008). All my circuits: using multiple electrodes to understand functioning neural networks. *Neuron* *60*, 483–488.
- Mountcastle, V.B., Reitboeck, H.J., Poggio, G.F., and Steinmetz, M.A. (1991). Adaptation of the Reitboeck method of multiple microelectrode recording to the neocortex of the waking monkey. *J. Neurosci. Methods* *36*, 77–84.
- Mulliken, G.H., Bichot, N.P., Ghadooshahy, A., Sharma, J., Kornblith, S., Philcock, M., and Desimone, R. (2015). Custom-fit radiolucent cranial implants for neurophysiological recording and stimulation. *J. Neurosci. Methods* *247*, 146–154.
- Musallam, S., Bak, M.J., Troyk, P.R., and Andersen, R.A. (2007). A floating metal microelectrode array for chronic implantation. *J. Neurosci. Methods* *160*, 122–127.
- Nguyen, D.P., Layton, S.P., Hale, G., Gomperts, S.N., Davidson, T.J., Kloosterman, F., and Wilson, M.A. (2009). Micro-drive array for chronic in vivo recording: tetrode assembly. *J. Vis. Exp.* (26), 1098, <https://doi.org/10.3791/1098>.
- Nicolelis, M.A., Ghazanfar, A.A., Faggin, B.M., Votaw, S., and Oliveira, L.M. (1997). Reconstructing the engram: simultaneous, multisite, many single neuron recordings. *Neuron* *18*, 529–537.
- Nicolelis, M.A., Dimitrov, D., Carmena, J.M., Crist, R., Lehew, G., Kralik, J.D., and Wise, S.P. (2003). Chronic, multisite, multielectrode recordings in macaque monkeys. *Proc. Natl. Acad. Sci. USA* *100*, 11041–11046.
- Nordhausen, C.T., Maynard, E.M., and Normann, R.A. (1996). Single unit recording capabilities of a 100 microelectrode array. *Brain Res.* *726*, 129–140.
- Power, J.D., Cohen, A.L., Nelson, S.M., Wig, G.S., Barnes, K.A., Church, J.A., Vogel, A.C., Laumann, T.O., Miezin, F.M., Schlaggar, B.L., and Petersen, S.E. (2011). Functional network organization of the human brain. *Neuron* *72*, 665–678.
- Prut, Y., Vaadia, E., Bergman, H., Haalman, I., Slovlin, H., and Abeles, M. (1998). Spatiotemporal structure of cortical activity: properties and behavioral relevance. *J. Neurophysiol.* *79*, 2857–2874.
- Purushothaman, G., Scott, B.B., and Bradley, D.C. (2006). An acute method for multielectrode recording from the interior of sulci and other deep brain areas. *J. Neurosci. Methods* *153*, 86–94.
- Roelfsema, P.R., Engel, A.K., König, P., and Singer, W. (1997). Visuomotor integration is associated with zero time-lag synchronization among cortical areas. *Nature* *385*, 157–161.
- Rossant, C., Kadir, S.N., Goodman, D.F.M., Schulman, J., Hunter, M.L.D., Saleem, A.B., Grosmark, A., Belluscio, M., Denfield, G.H., Ecker, A.S., et al. (2016). Spike sorting for large, dense electrode arrays. *Nat. Neurosci.* *19*, 634–641.
- Rousche, P.J., Pellinen, D.S., Pivin, D.P., Jr., Williams, J.C., Vetter, R.J., and Kipke, D.R. (2001). Flexible polyimide-based intracortical electrode arrays with bioactive capability. *IEEE Trans. Biomed. Eng.* *48*, 361–371.
- Rubinov, M., and Sporns, O. (2010). Complex network measures of brain connectivity: uses and interpretations. *Neuroimage* *52*, 1059–1069.
- Salazar, R.F., Dotson, N.M., Bressler, S.L., and Gray, C.M. (2012). Content-specific fronto-parietal synchronization during visual working memory. *Science* *338*, 1097–1100.
- Schwarz, D.A., Lebedev, M.A., Hanson, T.L., Dimitrov, D.F., Lehew, G., Meloy, J., Rajangam, S., Subramanian, V., Ifft, P.J., Li, Z., et al. (2014). Chronic, wireless recordings of large-scale brain activity in freely moving rhesus monkeys. *Nat. Methods* *11*, 670–676.
- Swadlow, H.A., Bereshpolova, Y., Bezdudnaya, T., Cano, M., and Stoelzel, C.R. (2005). A multi-channel, implantable microdrive system for use with sharp, ultra-fine “Reitboeck” microelectrodes. *J. Neurophysiol.* *93*, 2959–2965.
- Szabó, I., Czurkó, A., Csicsvari, J., Hirase, H., Leinekugel, X., and Buzsáki, G. (2001). The application of printed circuit board technology for fabrication of multi-channel micro-drives. *J. Neurosci. Methods* *105*, 105–110.
- Tass, P., Rosenblum, M.G., Weule, J., Kurths, J., Pikovsky, A., Volkman, J., Schnitzler, A., and Freund, H.J. (1998). Detection of n:m phase locking from noisy data: application to magnetoencephalography. *Phys. Rev. Lett.* *81*, 3291.
- Tolias, A.S., Ecker, A.S., Siapas, A.G., Hoenselaar, A., Keliris, G.A., and Logothetis, N.K. (2007). Recording chronically from the same neurons in awake, behaving primates. *J. Neurophysiol.* *98*, 3780–3790.
- Van Essen, D.C. (2012). Cortical cartography and Caret software. *Neuroimage* *62*, 757–764.

- Venkatachalam, S., Fee, M.S., and Kleinfeld, D. (1999). Ultra-miniature headstage with 6-channel drive and vacuum-assisted micro-wire implantation for chronic recording from the neocortex. *J. Neurosci. Methods* *90*, 37–46.
- Vetter, R.J., Williams, J.C., Hetke, J.F., Nunamaker, E.A., and Kipke, D.R. (2004). Chronic neural recording using silicon-substrate microelectrode arrays implanted in cerebral cortex. *IEEE Trans. Biomed. Eng.* *51*, 896–904.
- Vos, B.P., Wijnants, M., Taeymans, S., and De Schutter, E. (1999). Miniature carrier with six independently moveable electrodes for recording of multiple single-units in the cerebellar cortex of awake rats. *J. Neurosci. Methods* *94*, 19–26.
- Wilson, M.A., and McNaughton, B.L. (1993). Dynamics of the hippocampal ensemble code for space. *Science* *261*, 1055–1058.

STAR★METHODS

KEY RESOURCES TABLE

REAGENT or RESOURCE	SOURCE	IDENTIFIER
Software and Algorithms		
MATLAB	MathWorks	https://www.mathworks.com/ ; RRID: SCR_001622
Solidworks	Dassault Systems	http://www.solidworks.com/
Caret	Van Essen, 2012	http://brainvis.wustl.edu/wiki/index.php/Main_Page ; RRID: SCR_006260
MonkeyLogic	Asaad and Eskandar, 2008a, 2008b	http://www.brown.edu/Research/monkeylogic/
Cheetah	Neuralynx	https://neuralynx.com/
Other		
256-Channel Digital Lynx System	Neuralynx	https://neuralynx.com/
Microelectrodes (Tungsten-in-Glass): exposed end (0.1"), wire dia (0.005", 125 μm), glass shaft dia. (0.0098", 250 μm), 60° taper angle, impedance at 1 kHz (~1.0 MΩ)	Alpha Omega	https://www.alphaomega-eng.com/

CONTACT FOR REAGENT AND RESOURCE SHARING

Further information and requests for resources and reagents should be directed to and will be fulfilled by the Lead Contact, Charles M. Gray (cmgray.montana@gmail.com).

EXPERIMENTAL MODEL AND SUBJECT DETAILS

Subjects

Data was collected from two adult female macaque monkeys. All procedures were performed in accordance with NIH guidelines and the Institutional Animal Care and Use Committee of Montana State University. The monkeys were head fixed using a cranial head post (Gray Matter Research), and positioned 57 cm from a 19-inch monitor.

METHOD DETAILS

Behavioral Task

We used MonkeyLogic software to run the experiment and record the eye position (Asaad and Eskandar, 2008a, 2008b). Eye position was monitored using an infrared eye-tracking system (240 Hz; ISCAN, Inc.). Eye signals were recorded and converted to degrees of visual angle (dva) by MonkeyLogic. A trial begins when the monkey acquires and holds fixation on a small fixation spot (fixation window = 3 dva). At a latency of 500 ms for monkey 1 or 800 ms for monkey 2, one of five possible sample images (size: 2.4x2.4 dva) is presented for 500 ms in the center of the screen (obscuring the fixation point). During the sample period the monkey has to maintain its gaze in the same 3 dva window used during the fixation period. The sample stimulus is followed by a randomized delay, 800-1200 ms for monkey 1 and 1000-1500 ms for monkey 2, in which no stimulus is present. At the end of the delay period, the fixation target is extinguished and the matching image and a non-matching image (one of the four other images) appear 5 dva from the center of the screen. For monkey 1, the match and non-match were always placed across from each other on the horizontal plane. The location (left or right) of the match and non-match were randomized on each trial. For monkey 2, the images were aligned either vertically, horizontally or diagonally. The location of the match and non-match and the alignment was randomly chosen on each trial. While the match image is visible, the monkey must make a saccadic eye movement to the matching image and maintain fixation for a brief period of time (200 ms for monkey 1 and 500 ms for monkey 2). Correct trials were rewarded with a drop of juice.

Chamber System

All custom components were designed using the Solidworks CAD package (Dassault Systems). The recording systems were designed to fit each animal by creating a 3D model of each animal's skull. To achieve this, we constructed an MRI-based 3D graphical model of each monkey's skull using Solidworks (Figure S1). Coronal sections were taken at 2 mm intervals spanning the infra-orbital and occipital ridges. We outlined the external surface of the skull and the internal surface of the cranial vault in each section using a spline interpolation algorithm. Successive outlines were linked to form a solid 3D model. We delineated the internal dimensions of the

chamber using the outer boundaries of the cerebral hemisphere to define a closed contour on the surface of the model. The chamber wall was 0.1" thick and its bottom surface was matched to the cranial surface at all locations. In some locations this caused the external boundary of the chamber to extend too far, so we reduced the dimensions to obtain a suitable fit to the skull. In design 2, we introduced sealed ports in the chamber wall to enable the sampling or release of fluids inside the chamber and the introduction of disinfectants or antibiotics.

Electrophysiological Recordings

Broadband signals (0.1 Hz - 9 kHz, sampled at 32 kHz) were recorded using a 256-channel Digital Lynx system (Neuralynx). Signals were lowpass filtered (1-100 Hz) and down-sampled to 1 kHz to obtain the local field potential (LFP). Spike sorting was performed in a similar manner as in earlier studies (Salazar et al., 2012; Dotson et al., 2014). First, broadband signals were highpass filtered (monkey 1: 500 Hz - 9 kHz; monkey 2: 500 Hz - 4 kHz). Second, a threshold of 5 standard deviations of the background signal was used to identify spikes. 32 data points were saved for each spike (11 points before and 21 points after and including the minimum). Waveforms were clustered using KlustaKwik (Rossant et al., 2016). Clusters were merged and artifacts were discarded using MClust (<http://redishlab.neuroscience.umn.edu/MClust/MClust.html>). To be considered a single unit (SUA), waveforms in the cluster were required to be stable over time, non-overlapping with all other clusters, and have an inter-spike interval histogram with a clear refractory period.

Anatomical Reconstruction Technique for Monkey 1

Following perfusion, the brain was removed, and sunk in a solution of fixative with 30% sucrose several days before being sectioned (60 μ m) and stained for Nissl substance (FD Neurotechnologies). To reconstruct the brain, the stained sections were photographed and then imported into Free-D (Andrey and Maurin, 2005). Sections were manually registered and then electrolytic lesions and microelectrode tracks were marked on the images. This information provided a 3D reconstruction of all the microelectrode tracks. We used this information and the record of microelectrode depths to estimate the microelectrode tip position and identify the recording locations of each microelectrode on each recording session.

QUANTIFICATION AND STATISTICAL ANALYSIS

Network Analysis

The data used in the network analysis was collected during a single recording session from monkey 2 (106 total signals). Data is from areas 7A, 7B, 8B, 8L, 8M, 8r, AIP, DP, F1, F2, F6, F7, LIP, MT, TPT, V1, V2, V6A, 1, 2, 3, 5, 24c, 44, 45B, and 46D. The phase locking analysis was performed on a 400ms window during the delay period, starting 400ms after the sample offset.

The phase locking analysis was implemented following Tass et al. (1998). First, each signal was bandpass filtered (zero phase forward and reverse digital IIR fourth order Butterworth filter) in 3 Hz steps with a 5 Hz band from 3 to 90 Hz, and then down sampled to 200 Hz. Next, the Hilbert transform was applied to extract time series of the instantaneous phase angles $[\phi(t)]$. Then, using the instantaneous phase angles, we calculated the distribution of relative phase angles $[\Psi = (\phi_1 - \phi_2) \bmod 2\pi]$ between each pair of signals. The resulting data was binned from 0° to 360° in 10° bins ($N = 36$ bins). The phase locking value $[PLV = (S_{max} - S) / S_{max}]$ was then calculated using Shannon entropy (S), where $S = -\sum_{i=1}^N P(i) \log_2 P(i)$, and $P(i)$ is the probability of observing a relative phase angle in each bin. The maximum entropy (S_{max}) is calculated as $[S_{max} = \log_2(N)]$.

We assessed the statistical significance of each phase locking value by comparing the observed PLV values to surrogate distributions. Surrogates were created by randomizing trial labels and then computing the PLV. Each surrogate distribution (200 surrogates) was fit with a generalized extreme value function in order to estimate p values less than 0.005 (smallest p value using just the surrogate distribution is $1/200 = 0.005$). Phase locking values between LFPs are typically much larger than shuffled surrogates (Antzoulatos and Miller, 2014). If the synchronized activity is not locked to task events, then the phase locking values estimated from trial shuffled data are very small. To account for this, we chose a very small significance threshold of $p < 0.000001$, which is slightly smaller than what would have been chosen based on Bonferroni correction for each functional connectivity network (with 106 nodes there are 5,565 pairs of signals; with a desired significance threshold of $p < .05$, the Bonferroni corrected threshold is $0.05/5,565 = 0.000009$). Although we found that the exact significance threshold made little difference, it did help to prevent noisy data points from entering the analysis. For the functional connectivity analysis, if multiple PLVs were significant within a frequency range, then the PLV with the highest magnitude and the corresponding relative phase angle was used.

The modularity analysis was performed using the Brain Connectivity Toolbox (Rubinov and Sporns, 2010). Graph theoretic analyses typically explore network properties using a range of magnitude thresholds for a given metric, which enables the exploration of high density to low density networks (Bassett et al., 2008; Bullmore and Bassett, 2011; Power et al., 2011). Subsequently, after selecting data points for significance based on the trial shuffled data, we used multiple magnitude thresholds based on the PLVs. This allowed us to quantify how the modularity changes as a function of network density and to determine whether our results are robust to the chosen parameters. Undirected binary graphs were created using the results from the phase locking analysis. Network visualization was performed in the software package Gephi using force atlas and a built in modularity analysis (Bastian et al., 2009; Jacomy et al., 2014).

Neuron, Volume 96

Supplemental Information

**A Large-Scale Semi-Chronic
Microdrive Recording System
for Non-Human Primates**

Nicholas M. Dotson, Steven J. Hoffman, Baldwin Goodell, and Charles M. Gray

Supplemental Information

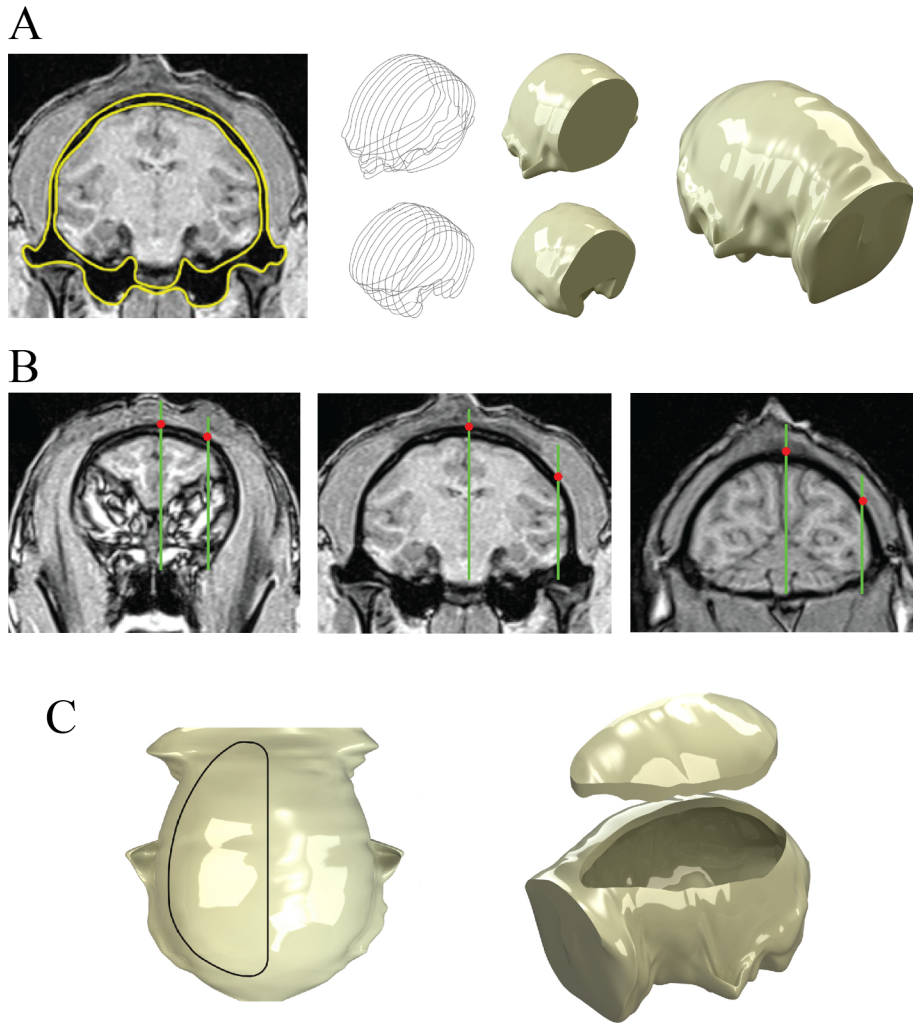


Figure S1. Design of the skull model and definition of the chamber boundaries (related to Figure 1).

A) The left image shows a coronal section of the MRI with outlines of the inner and outer boundaries of the skull in yellow. A sequence of the inner and outer outlines (8 shown) are linked, converted to their respective solid models, and subtracted from one another to yield the final 3D model of the skull (right). B) To define the boundary of the internal chamber wall the lateral and medial edges are marked in each coronal MRI section (three examples shown). The green lines mark the boundaries and the red circles mark the junctions of these lines on the skull surface. C) Dorsal and lateral views of the 3D skull model with the boundaries of the craniotomy outlined in black (left) along with an exploded view of the intended craniotomy (right).

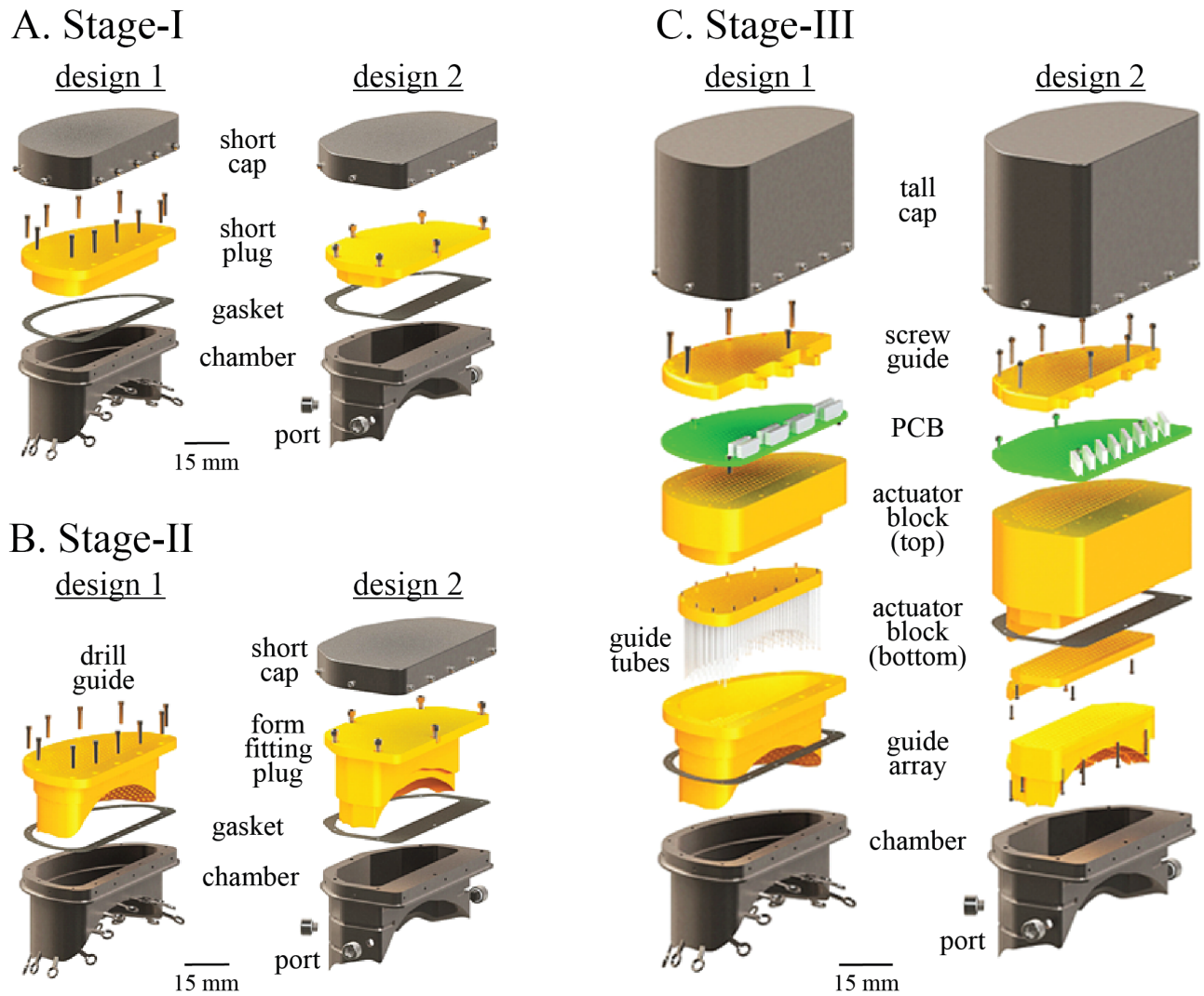


Figure S2. Exploded views of the design drawings of the large-scale chamber and microdrive systems for each of the three stages of design 1 and design 2 (related to Figure 1). A) Stage I designs illustrating the chamber, short plug and protective cap. B) Stage II designs illustrating the drill guide and chamber for design 1 (left) and the chamber, form-fitting plug and protective cap for design 2. C) Stage III design drawings showing the relationships between the microdrive components and the chambers and protective caps.

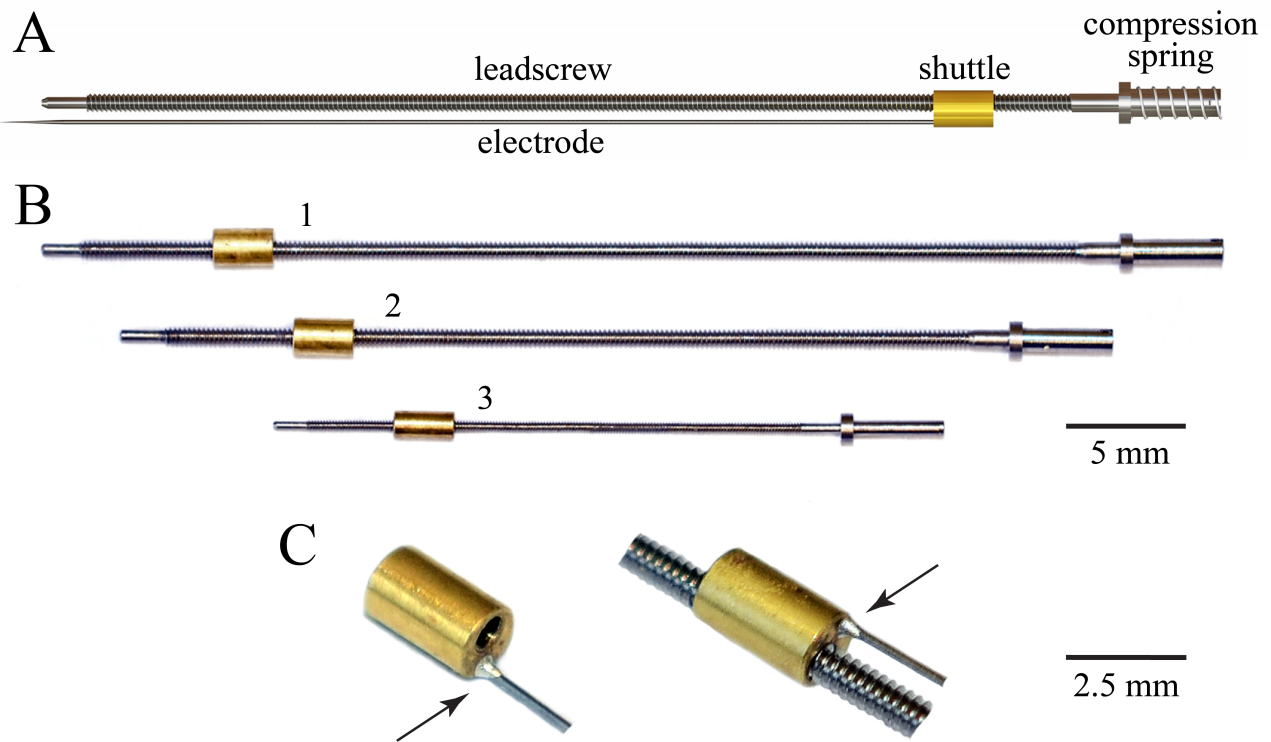


Figure S3. Actuator mechanism (related to Figure 1). A) Design drawing of the actuator showing the relationships between the leadscrew, shuttle and compression spring. B) Photographs of the three different leadscrews and two types of shuttles using in the two designs. The 41 mm and 33 mm leadscrews used in design 2 are shown in 1 and 2, respectively. The 20 mm leadscrew and associated shuttle used in design 1 are shown in 3. C) Photographs illustrating the bonding of the electrode to the brass shuttle using a heat-treated conductive epoxy (arrows).

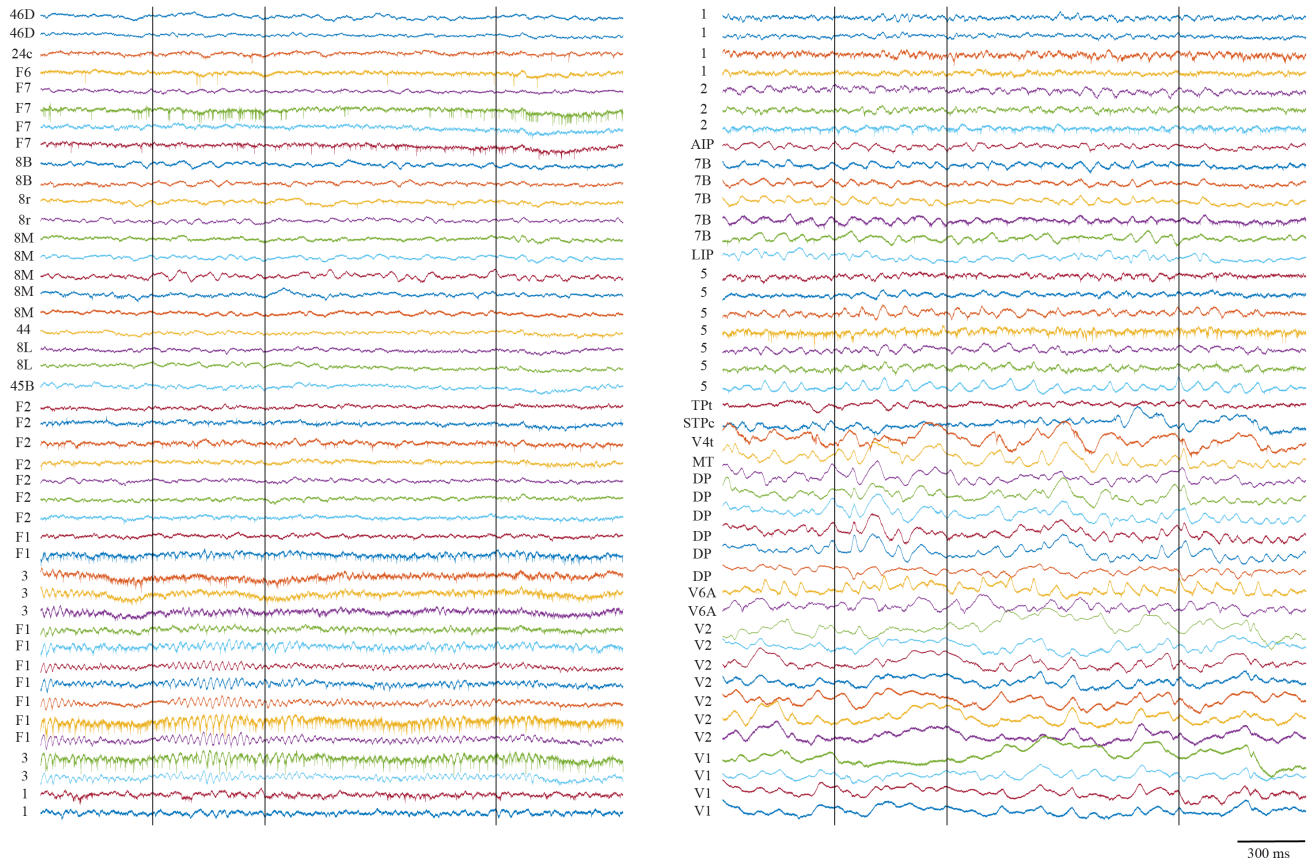


Figure S4. Broadband data simultaneously sampled from 88 microelectrodes in monkey 2 for the full duration of the trial shown in Figure 4. The cortical area of each recording is indicated just to the left of each trace according to the nomenclature of Markov et al. (2014). The black vertical lines indicate the sample onset, sample offset, and the match onset.

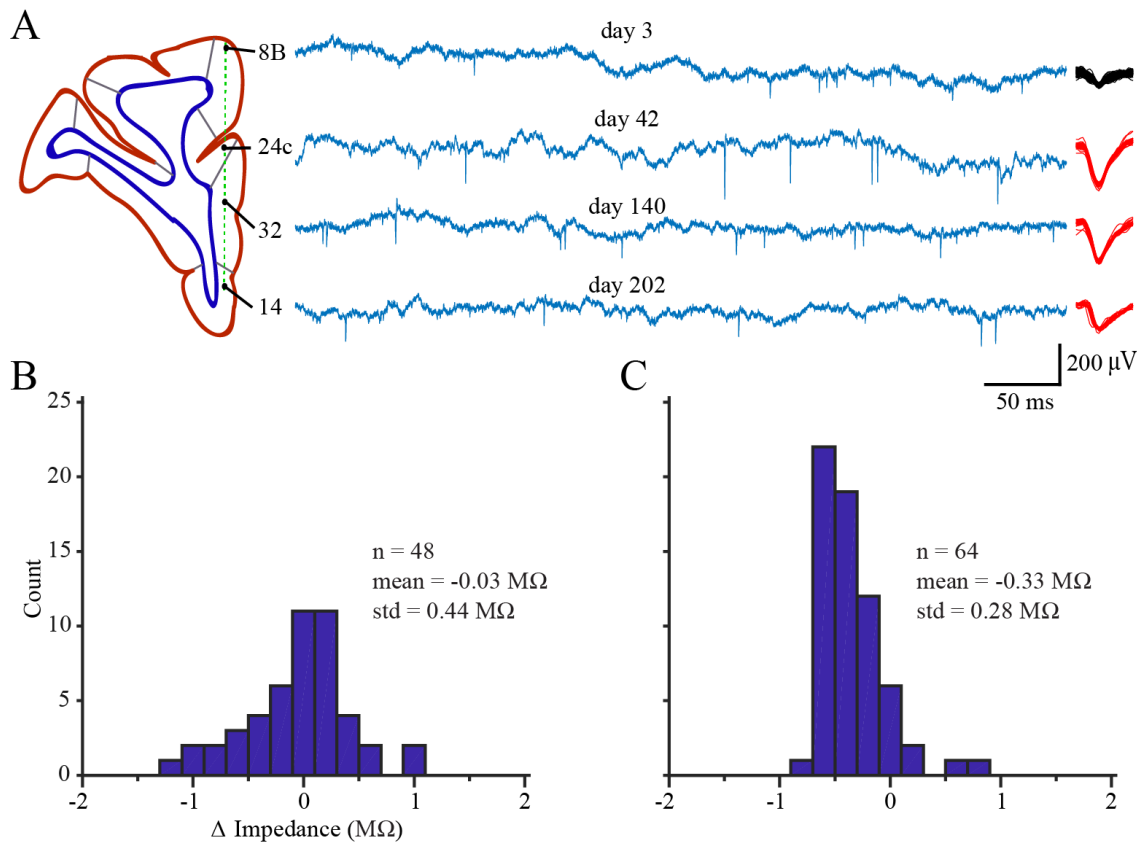


Figure S5. Recording quality over time for a single electrode and the changes in electrode impedance across the experiments (related to Figure 6). A) The image on the left shows the outline of a coronal section through the prefrontal cortex with areal boundaries indicated by grey lines according to Markov et al. (2014). The dashed green line shows the path of a reconstructed electrode track. The points marked on the track indicate the recording locations for the four raw data traces shown in the middle of the plot. These signals were recorded in monkey 2 on chronological days 3, 42, 140 and 202, sampled from areas 8B, 24c, 32 and 14, respectively. The plots on the right show 100 superimposed waveforms extracted from each recording (MUA (black) and SUA (red)). B,C) Histograms of the difference in electrode impedance from the last set of impedance measurements relative to the first set, for all applicable electrodes in Monkey 1 (B) and Monkey 2 (C). Data were restricted to functioning electrodes with impedance values ranging between 0.2 to 1.5 $M\Omega$. There are a wide range of changes in impedance in both experiments, and a consistent reduction in impedance in monkey 2 of ~ 330 k Ω .